PHYSICAL REVIEW A **66**, 063417 (2002)

Role of long quantum orbits in high-order harmonic generation

D. B. Milošević[1,2] and W. Becker[2,*]
[1]*Faculty of Science, University of Sarajevo, Zmaja od Bosne 35, 71000 Sarajevo, Bosnia and Herzegovina*
[2]*Max-Born-Institut, Max-Born-Strasse 2a, 12489 Berlin, Germany*

(Received 26 August 2002; published 31 December 2002)

Single-atom high-order harmonic generation is considered in the strong-field approximation, as formulated in the Lewenstein model, and analyzed in terms of quantum orbits. Orbits are classified according to the solutions of the saddle-point equations. The results of a numerical integration are compared with the saddle-point approximation and the uniform approximation. Approximate analytical solutions for long orbits are presented. The formalism developed is used to analyze the enhancement of high-order harmonic generation near channel closings. The enhancements exactly at the channel closings are extremely narrow and built up by the constructive interference of a very large number of quantum orbits. Additional broader enhancements occur slightly below channel closings. They are generated by the interplay of a medium number of orbits.

DOI: 10.1103/PhysRevA.66.063417 PACS number(s): 32.80.Rm, 42.65.Ky, 42.50.Hz

I. INTRODUCTION

The study of intense-laser-atom physics is of current importance both in science and technology [1–4]. High-order harmonic generation (HHG) and above-threshold ionization (ATI) are the two processes most studied in intense-laser-atom physics. In these processes, the atomic electron absorbs and emits a large number of laser photons in many different time orders so that the number of pathways in quantum-mechanical-state space that connect the initial and the final quantum states is enormous. The number of relevant pathways is drastically lower from the point of view of ''quantum orbits'' [1,4–8]. These come about in a semiclassical approximation of the relevant transition amplitudes, which is very well justified for the intense laser fields of interest. Quantum orbits are closely related to the space-time trajectories of classical particles. To a given harmonic in HHG or final electron momentum in ATI, many quantum orbits contribute, which differ in the times when they enter the continuum by ionization and the later times when they recombine or rescatter. The time in between ionization and recombination can amount to very many cycles of the laser field. Quantum mechanics is hidden in this picture in two ways: the contributions of the various orbits are superposed in the fashion of Feynman's path integral, and they are complex to account for the tunneling nature of the initial step of the HHG and ATI processes.

Usually, and this has rendered quantum orbits an extremely useful tool for the analysis of various aspects of HHG [1], only very few orbits need be considered, as few as two or even one. This is so, in particular, for the upper part of the HHG plateau and its cutoff region. This paper will be concerned with situations where this is not so, which is the case for certain intensities and in the middle and the low-energy part of the plateau. The analysis of experimental data as well as numerical simulations in terms of quantum paths [9] have been instrumental for the understanding of HHG [10,11]. Recently, these techniques have been employed to generate HHG pulses with specific objectives via tayloring the driving laser pulse [12].

One of the most interesting features of the low-energy part of the plateau is a resonancelike enhancement: a small variation of the laser-field intensity by just a few percent can induce enhancements of particular harmonics of up to one order of magnitude. Such enhancements have been observed experimentally for ATI [13–16] and also for HHG [17], and various theoretical arguments have been put forward for their explanation [16–24]. Some of them [18,19] attribute these features to the multiphoton resonance of the ground state and high-lying ponderomotively upshifted Rydberg states. An apparently different view relates these enhancements to channel closings and threshold anomalies [16,20–24]. In the presence of the laser field, the continuum states are upshifted by the ponderomotive energy U_{P}, so that ionization can occur only after the absorption of $n>(I_{\mathrm{P}}+U_{\mathrm{P}})/\hbar\omega$ photons of energy $\hbar\omega$, where I_{P} is the atomic ionization energy. With increasing laser-field intensity, U_{P} also increases, until n-photon ionization is no longer possible, and $n+1$ photons are required. We refer to this as the nth-channel closing. If the laser intensity corresponds exactly to this channel closing, the electron is released in the continuum with zero drift momentum so that, during its ensuing oscillatory motion in the laser field, it can revisit its parent ion many times before it recombines or rescatters.

In the quantum-orbits formalism, this means there are many corresponding probability amplitudes that interfere. Constructive interference of these amplitudes will manifest itself as an enhancement in the HHG or high-order ATI spectra. Recently, for the case of high-order ATI in the context of the improved Keldysh model, Popruzhenko *et al.* [24] have shown analytically that the interference can be constructive at channel closings and have discussed, under which conditions it has the most pronounced consequences. One of the aims of the present paper is to extend this analysis to HHG. A complementary approach [22,23], which is based on the exact solutions for the HHG and ATI transition amplitudes in the case of the zero-range potential model, relates these enhancements to the well-known threshold anomalies [25,26],

---

[*] Also at Center for Advanced Studies, Department of Physics and Astronomy, University of New Mexico, Albuquerque, NM 87131.

1050-2947/2002/66(6)/063417(14)/$20.00

which occur whenever, as a function of some parameter, channels open or close.

These resonancelike features have been observed earlier in nonperturbative numerical calculations of ATI spectra [27] and for HHG using the zero-range potential model [28–31]. It should be mentioned that strong intensity-dependent resonant enhancements of high-order harmonics have also been predicted to occur due to one-photon or multiphoton field-atom resonances [32–34]. They are outside the scope of the strong-field approximation and the Lewenstein model, and will not be considered here.

In the present paper, we will develop various approximations for the calculation of high-order harmonic emission, starting, in Sec. II, from an efficient numerical scheme based on the fast Fourier transform and numerical integration over the electron travel time, up to simple analytical expressions in Sec. V that can be used to explain the resonancelike enhancements at the channel closings. In Sec. III, we present the saddle-point approximation (SPA). Special attention is devoted to the classification of the quantum orbits, where we follow the scheme introduced for high-order ATI [24], and to some characteristics of the low-order harmonics that have not been explored before. In Sec. IV, the so-called uniform approximation is introduced. This approximation is an improvement of the SPA, which works well also in the cutoff region of a given quantum orbit where the SPA fails [35]. This is of crucial importance in the case, where many orbits interfere so that the spikes at the cutoffs in the harmonic spectrum that are produced by the SPA can accumulate, leading to erroneous results. In Sec. V, we present approximate analytical solutions of the SPA equations, which, in a natural way, lead to the above-mentioned classification of the quantum orbits. Similar analytical solutions of the saddle-point equations were recently used to explain the enhancement at the channel closings for ATI in Ref. [24]. These solutions are particularly useful in the limit of long orbits, so that we make use of them in Sec. VI to consider the resonant enhancement of HHG at the channel closings. Both the simple analytical formulas and various numerical results that explain this effect will be presented. In Sec. VII, further examples that illustrate the power of the developed formalism will be discussed.

II. HARMONIC-EMISSION RATE FOR ZERO-RANGE POTENTIAL

For a linearly polarized laser field with period $T=2\pi/\omega$, the nth-harmonic-emission rate (in a.u.) [4,36] is

$$w_n=\frac{1}{2\pi}\left(\frac{n\omega}{c}\right)^3|T_n|^2,\quad T_n=\int_0^T\frac{dt}{T}e^{in\omega t}d(t),\tag{1}$$

where T_n is the T-matrix element and $d(t)$ is the time-dependent dipole matrix element. We will consider a monochromatic field with the vector potential

$$\mathbf{A}(t)=A(t)\hat{\mathbf{e}}_x,\quad A(t)=A\cos\omega t.\tag{2}$$

We use the strong-field approximation [37] and its realization in the Lewenstein model [5] as well as a zero-range binding potential [29,38,39], and approximate $d(t)$ [40] by

$$\begin{aligned}d(t)&\approx\int dt_0\langle\psi_0(t)|xG_L^{(+)}(t,t_0)V|\psi_0(t_0)\rangle\\&=-i\int d^3q\langle\psi_0|x|\mathbf{q}+\mathbf{A}(t)\rangle\\&\quad\times\int_{-\infty}^{t}dt_0e^{iS(\mathbf{q};t,t_0)}\langle\mathbf{q}+\mathbf{A}(t_0)|V|\psi_0\rangle,\end{aligned}\tag{3}$$

where G_L is the Volkov propagator in the length gauge, $V(\mathbf{r})=(2\pi/\kappa)\delta(\mathbf{r})(\partial/\partial r)r$ is the zero-range potential, $\langle\mathbf{r}|\psi_0(t)\rangle=\psi_0(\mathbf{r})\exp(iI_\mathrm{P}t)=[\kappa/(2\pi)]^{1/2}\exp(-\kappa r+iI_\mathrm{P}t)/r$ is the atomic ground state for the zero-range potential in the absence of the laser field, $I_\mathrm{P}=\kappa^2/2$ is the ionization energy, and

$$S(\mathbf{q};t,t_0)=-\int_{t_0}^{t}dt'\{[\mathbf{q}+\mathbf{A}(t')]^2/2+I_\mathrm{P}\}\tag{4}$$

is the quasiclassical action. The matrix elements in the dipole matrix element (3) are

$$\langle\mathbf{q}|V|\psi_0\rangle=-\frac{\kappa^{1/2}}{2\pi},\quad\langle\psi_0|x|\mathbf{q}\rangle=\frac{2iq_x\kappa^{1/2}}{\pi(q^2+\kappa^2)^2}.\tag{5}$$

The integral over d^3q in Eq. (3) can be solved using the method of Ref. [41]. For the field (2), the condition $\boldsymbol{\nabla}_\mathbf{q}S=\mathbf{0}$ yields the momentum $q_{sx}=A(\sin\omega t_0-\sin\omega t)/[\omega(t-t_0)]$, $q_{sy}=q_{sz}=0$, for which the action is stationary. As the final result, we obtain

$$\begin{aligned}w_n=\frac{I_\mathrm{P}}{8\pi^2}\left(\frac{n\omega}{cU_\mathrm{P}}\right)^3\Bigg|\int_0^T\frac{dt}{T}e^{in\omega t}\\\times\int_0^\infty\frac{d\tau}{\tau^{3/2}}\frac{(k+\cos\omega t)\exp(iS_s)}{[(k+\cos\omega t)^2+\gamma^2]^2}\Bigg|^2,\end{aligned}\tag{6}$$

where $U_\mathrm{P}=A^2/4$ is the ponderomotive energy, $\gamma=\sqrt{2I_\mathrm{P}/A^2}$ is the Keldysh parameter, $k=q_{sx}/A$, and the stationary action in the exponent is $S_s\equiv S(\mathbf{q}_s;t,t_0)$. The integral over the travel time $\tau=t-t_0$ in Eq. (6) is solved by numerical integration. The harmonic spectrum is then obtained by the fast Fourier-transform method.

III. SADDLE-POINT APPROXIMATION

The harmonic-emission rate (6) has been obtained by applying the saddle-point method to the *three-dimensional* integral over d^3q. Application of the SPA to the *five-dimensional* integral over d^3q, dt, and dt_0 yields a much simplified expression [4,7,8]: The stationarity conditions that the first derivatives $\partial/\partial\mathbf{q}$, $\partial/\partial t$, and $\partial/\partial t_0$ of the exponent $S(\mathbf{q};t,t_0)+n\omega t$ in the integrand be equal to zero lead to the following system of equations for the variables $k=q_x/A$, $\varphi=\omega t$, and $\varphi_0=\omega t_0$:

$$k(\varphi-\varphi_0)+\sin\varphi-\sin\varphi_0=0, \tag{7a}$$

$$(k+\cos\varphi)^2=\gamma_n^2, \tag{7b}$$

$$(k+\cos\varphi_0)^2=-\gamma^2, \tag{7c}$$

where $\gamma_n^2=(n\omega-I_{\mathrm{P}})/(2U_{\mathrm{P}})$. The five-dimensional integral then reduces to a sum over solutions $(k_s,\varphi_s,\varphi_{0s})$ of the system (7), and we get

$$w_n=\frac{1}{n\omega}\left(\frac{\omega}{c}\right)^3\left(\frac{\gamma}{2\pi}\right)^2\left|\sum_s A_{ns}e^{iS_{ns}}\right|^2, \tag{8}$$

where

$$A_n(k,\varphi,\varphi_0)=\frac{k+\cos\varphi}{(\varphi-\varphi_0)F_n^{1/2}}, \tag{9}$$

$$S_n(k,\varphi,\varphi_0)=(2U_{\mathrm{P}}k^2-U_{\mathrm{P}}-I_{\mathrm{P}})\frac{\varphi-\varphi_0}{\omega} -\frac{U_{\mathrm{P}}}{2\omega}(\sin 2\varphi-\sin 2\varphi_0)+n\varphi, \tag{10}$$

and F_n is determined by the determinant

$$\left(\frac{\partial^2 S_n}{\partial\varphi\partial\varphi_0}\right)^2-\frac{\partial^2 S_n}{\partial\varphi_0^2}\frac{\partial^2 S_n}{\partial\varphi^2}=\left(\frac{4U_{\mathrm{P}}}{\omega}\right)^2\frac{F_n(k,\varphi,\varphi_0)}{\varphi-\varphi_0},$$

so that

$$F_n(k,\varphi,\varphi_0)=(k+\cos\varphi)(k+\cos\varphi_0)[(k^2+\sin\varphi\sin\varphi_0)\times(\varphi-\varphi_0)-\sin(\varphi-\varphi_0)]. \tag{11}$$

In the rate (8), we used the notation $A_{ns}\equiv A_n(k_s,\varphi_s,\varphi_{0s})$, and similarly for S_n and F_n.

Introducing the solution for $k=k(\varphi,\varphi_0)$ from Eq. (7a) into Eqs. (7b) and (7c), we obtain a system of two equations, which can be solved numerically for the complex variables φ and φ_0. In Fig. 1, examples of these solutions are presented. The left-hand panels display $\mathrm{Im}\varphi_0$ as functions of $\mathrm{Re}\varphi_0$, the right-hand panels $\mathrm{Im}\varphi$ as functions of $\mathrm{Re}\varphi$. The harmonic order n changes as a continuous parameter along each curve. The corresponding values of n, are indicated at the beginning and at the end of each particular solution. Also indicated are the values of n for which different solutions approach each other most closely. These values correspond to the cutoff of the harmonic spectrum that is generated by this particular pair of solutions [see Fig. 4(a)].

To characterize the various solutions of the saddle-point equations (7), we use a multiindex consisting of the three numbers $\alpha\beta m$, similarly as in Ref. [24]. This notation is explained in detail in Sec. V, but we summarize it in Fig. 2. Briefly, for return times t within one cycle of the field, e.g., $0\leqslant t<T$, there are infinitely many pairs of solutions, which can be ordered by their start time t_0. For $-(m+1/2)T\leqslant t_0<-(m-1/2)T$, where $m=0,1,2,\ldots$, there are two pairs of solutions. The pair having the longer (shorter) travel time $t-t_0$ carries the index $\beta=-1$ $(\beta=+1)$. Each pair again consists of two orbits with slightly different travel times (this is well known from the Lewenstein model [5] of HHG), and we discriminate the longer from the shorter orbit by the index α, as indicated. The index m gives the approximate length of the travel time in multiples of the laser period, $m=[(t-t_0)/T]$ (with $[x]$ the largest integer $\leqslant x$). For $m=0$, there is only one pair of solutions, having $\beta=-1$. In addition, there is one solution with a very short travel time, which we denote by L (see the top panels of Fig. 1). The solution L is responsible for the low-order harmonic spectrum, it does not contribute to the harmonics with $n>I_{\mathrm{P}}/\omega$. For all other solutions, the imaginary part of the variable $\varphi=\omega t$ is very small, while its real part lies in the interval $[0,2\pi]$.

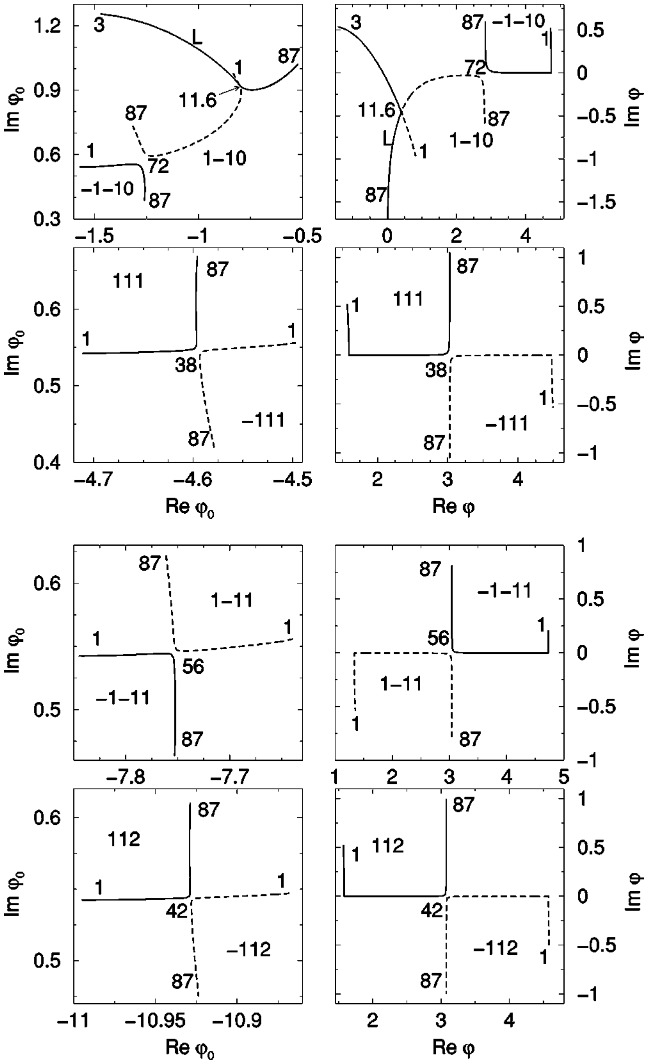

FIG. 1. Solutions of the saddle-point equations for HHG by a hydrogen atom (ionization energy $I_{\mathrm{P}}=13.6$ eV) with a linearly polarized laser field having the intensity 2×10^{14} W/cm^2 and the photon energy 1.17 eV. The solutions are labeled by the numbers $\alpha\beta m$ (cf. Fig. 2) and by the corresponding harmonic orders n, as explained in the text. The solutions, whose contributions have to be discarded after their respective cutoffs are indicated by dashed lines.

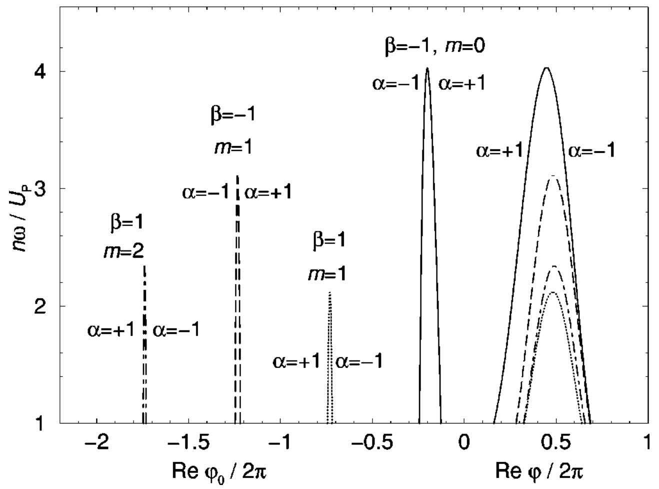

FIG. 2. Examples of the notation $\alpha\beta m$ used to label the solutions of the saddle-point equations (7). The solid, long-dashed, dot-dashed, and dotted curves in the right-hand part of the figure specify the return times for the four pairs of orbits with the shortest travel times. In the left-hand part of the figure, the counterpart of each curve identifies the corresponding start times. The harmonic photon energy in multiples of U_P is plotted on the ordinate, and horizontal lines (at constant energy) relate start times and return times for the respective orbits. There are infinitely many further solutions that have start times t_0 beyond the left-hand margin of the figure. Their maximal return energies converge to I_P+2U_P. The curves have been calculated for the same laser and atomic parameters as in Fig. 1.

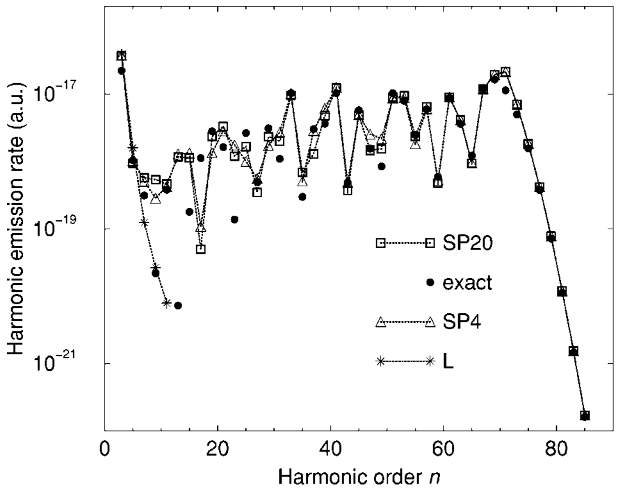

FIG. 3. Comparison of the harmonic spectrum obtained using numerical integration with the spectrum obtained using the saddle-point approximation. Harmonic-emission rates (in atomic units) are presented as functions of harmonic order for the same laser and atomic parameters as in Fig. 1. According to Refs. [5,42], the cutoff is at $n_{\max}\omega=1.325I_P+3.173U_P=72.3\omega$. The small filled circles represent the "exact" results obtained using Eq. (6), while the open symbols (connected by dashed lines) give the results of the saddle-point approximation (8) including four (triangles) or 20 (squares) pairs of orbits. The contribution of the single solution L from Fig. 1 is denoted by stars.

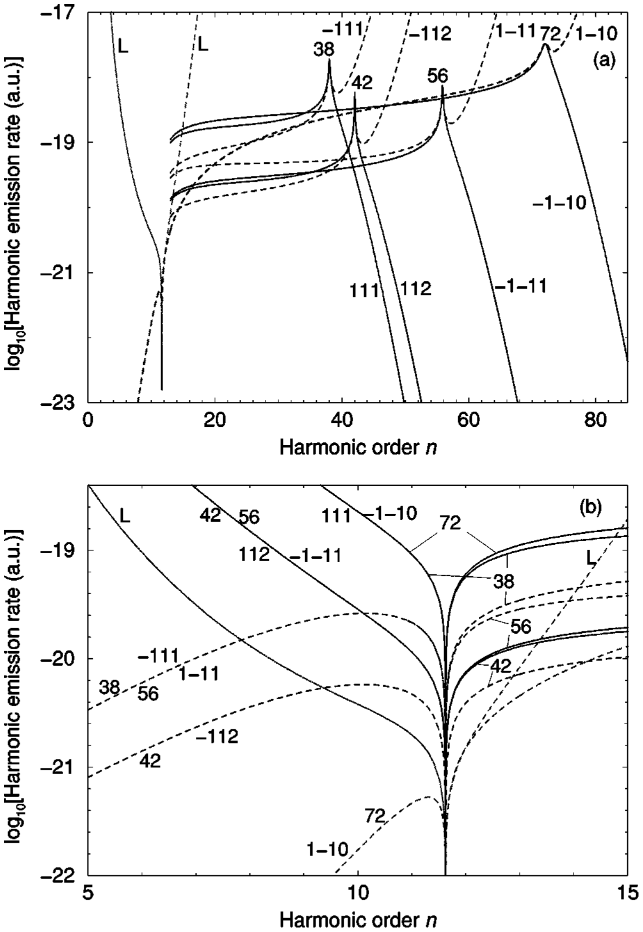

FIG. 4. Harmonic-emission rates for individual orbits as functions of the harmonic order for the same parameters as in Fig. 1. Each curve corresponds to one particular term of the sum (8), and is obtained using the saddle-point solutions that are presented in Fig. 1. The curves are denoted by the corresponding numbers $\alpha\beta m$ and by the cutoff harmonic orders n. The contributions presented by the dashed lines in panel (a) must be discarded after the cutoff. In panel (b), the partial harmonic-emission rates near the critical point $n\omega=I_P$ are presented. In panel (a), the solutions $\alpha\beta m$ are not shown below this critical point, except for 1−10.

In Fig. 3, we present the harmonic-emission rates as functions of the harmonic order for the laser and atomic parameters of Fig. 1. The results indicated by small filled circles are obtained using Eq. (6) (we refer to them as "exact"), while the large open symbols identify results obtained by the SPA formula (8). Open triangles (squares) exhibit the results that include 4 (20) pairs of the SPA solutions. For the low-order harmonics, both include the contribution of the solution L. The contribution of solely the solution L is denoted by the stars. For $n>I_P/\omega$, the contribution of the solution L has been dropped. The agreement of the "exact" and the SPA results is very good, except for $n\propto I_P/\omega$.

In general, very few SPA solutions suffice to reproduce the "exact" spectrum. The pair of solutions $\pm1-10$ is essentially the only one to contribute to the part of the plateau preceding the cutoff and still dominates the remainder of the plateau, with the other solutions only making significant contributions near their respective cutoffs [43]. In Fig. 4, we present the harmonic spectrum that results from particular solutions $\alpha\beta m$ via the corresponding terms of the sum (8). The solutions are depicted in the various panels of Fig. 1. For the top panels, the cutoff is at $n=72$. After the cutoff, the contribution of the solution $\alpha\beta m=1$–10 (viz., the short orbit) must be discarded, so that for $n>72$, only the solution from -1–10 contributes to the spectrum. The situation is similar for the other pairs of solutions presented in Fig. 1. The solutions 111, from -1–11, and 112 correspond to the solid lines and the cutoffs at $n=38$, 56, and 42, respectively. The solutions -111, 1–11, and -112, denoted by dashed lines, have to be discarded after these cutoffs. An analog of Fig. 4(a) for high-order ATI can be found in Ref. [45].

The sharp spikes at these cutoffs suggest that the SPA fails near these values of n. This also shows, though less dramatically, in the discrepancy between the "exact" and the SPA results of Fig. 3 around the cutoffs. At and in the vicinity of these critical points, the uniform-asymptotic-expansion method to be explained below in Sec. IV gives adequate results [35].

More problematic is the critical point at $n\omega=I_{\mathrm{P}}$, for which the partial contribution of each saddle-point solution approaches zero, cf. Fig. 4(b). Indeed, the SPA results for values of $n\approx I_{\mathrm{P}}/\omega$ are not in good agreement with the ″exact″ results as can be seen in Fig. 3. From the right-hand top panel of Fig. 1, we see that the solution 1–10 exhibits, exactly at the point $I_{\mathrm{P}}/\omega=11.6$, an avoided crossing with the solution L. The solution L cannot be classified by the numbers $\alpha\beta m$. For low harmonics, it gives the main contribution to the harmonic spectrum, while for $n\omega>I_{\mathrm{P}}$, it has to be discarded (the dashed L-line in Fig. 4). The solutions $\alpha\beta m$ can be continued into the region $n\omega<I_{\mathrm{P}}$. This is shown in Fig. 4(b). The solutions represented by solid lines (except solution L) must be discarded from the sum (8) for $n\omega<I_{\mathrm{P}}$. The saddle-point solutions of Fig. 1 that correspond to the results of Fig. 4(b) can be identified by their onset at the harmonic order $n=1$. The corresponding values of the return time $\mathrm{Im}\varphi$ become large for $n<I_{\mathrm{P}}/\omega$, and are responsible for the swastikalike shape of the curve $\mathrm{Im}\varphi=f(\mathrm{Re}\varphi)$.

In order to get further insight into the physical meaning of the saddle-point solutions presented above, we will inspect the corresponding quantum orbits [4,7,8,42]. Solving the Newton equation for the electron in the laser field, we get $x(t)=x(t_0)+[v(t_0)-A(t_0)](t-t_0)$, where $x(t_0)$ and $v(t_0)$ are the initial electron coordinate and velocity, respectively. With $v(t_0)=q_{sx}+A(t_0)$ and $x(t_0)=0$, the orbits $x(t)$ are determined by the (complex) solutions of the saddle-point equations (7). We can relate their real parts to actual electron orbits traveled in space and time. They are

$$x_{ns}(\varphi_{\mathrm{R}})=\frac{A}{\omega}\mathrm{Re}[\sin\varphi_{\mathrm{R}}-\sin\varphi_{0s}+k_s(\varphi_{\mathrm{R}}-\varphi_{0s})],$$

$$(\mathrm{Re}\varphi_{0s}\leqslant\varphi_{\mathrm{R}}\leqslant\mathrm{Re}\varphi_s) \qquad (12)$$

as a function of the real time φ_R. That is, the electron is born at the end of the tunnel at the position $x_{ns}(\mathrm{Re}\varphi_{0s})$ then it moves in the laser field, and at the time $\mathrm{Re}\varphi_s/\omega$, it returns to the position of the ion, where it recombines emitting the nth harmonic. Notice that while $x_{ns}(\varphi_{0s})=x_{ns}(\varphi_s)=0$ for the complex saddle-point solutions φ_{0s} and φ_s, both $x_{ns}(\mathrm{Re}\varphi_{0s})$ and $x_{ns}(\mathrm{Re}\varphi_s)$ are nonzero. However, $x_{ns}(\mathrm{Re}\varphi_s)$ is very close to zero, in contrast to $x_{ns}(\mathrm{Re}\varphi_{0s})$, which typically is of the order of a few atomic units and specifies the end of the tunnel.

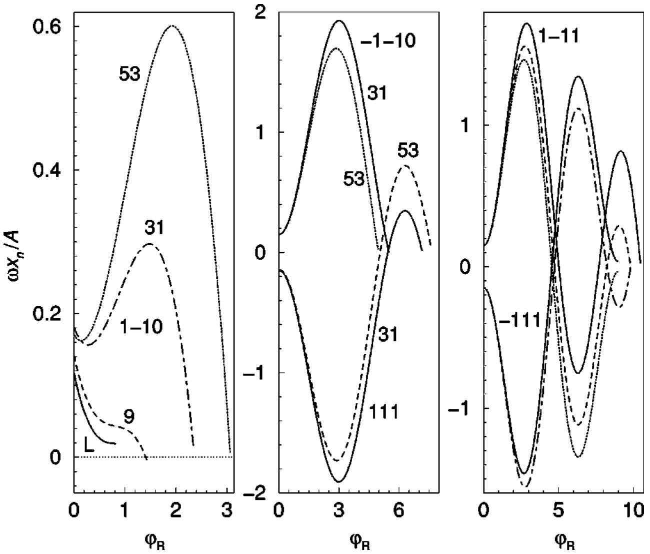

FIG. 5. Real parts of the quantum orbits, given by Eq. (12) and obtained using the saddle-point solutions of Fig. 1 for the 9th, 31st, and 53rd harmonics. The orbits are labeled by the corresponding numbers $\alpha\beta m$ and by the harmonic order n. The nontunneling low-harmonic-order orbits in the left-hand panel are denoted by the symbol L and the harmonic order $n=9$. In the right-hand panel, the harmonic orders presented are 9 (dotted curve), 31 (dashed curve), and 53 (solid curve) for $\alpha\beta m=1$–11, and $n=9$ (solid curve) and $n=31$ (dot-dashed curve) for $\alpha\beta m=-111$. In the right-hand panel, notice that, for given $\alpha\beta m$, the $n=9$ orbits approach the atomic core from the opposite side and with a smaller slope than those that produce the higher harmonics $n=31$ and $n=53$.

In Fig. 5, we display these orbits for various values of the harmonic order n and for various saddle-point solutions $s\equiv\alpha\beta m$. In the left-hand panel, the shortest orbit $\alpha\beta m=1$–10 is depicted for the harmonics $n=9$, 31, and 53, as well as the solution L for $n=9$. For $n=9$, both the solution L (solid curve) and the orbit $\alpha\beta m=1$–10 (dashed curve) describe an electron that is born at the end of the tunnel and moves straight back to the ionic core, never leaving the atom, but still acquiring enough energy to emit the ninth harmonic. All of the other orbits depicted in Fig. 5 correspond to the tunneling-recombination or three-step model of HHG. Along the longer orbits $(m=1)$, the electron revisits the atomic core more than once before it recombines.

For highly charged ions, the low-order part of the spectrum $(n<I_{\mathrm{P}}/\omega)$ can comprise hundreds of harmonics, which have been dubbed nontunneling harmonics, since their generation takes place entirely inside the atom [46]. For this case, a classical picture has been formulated that is able to describe this process. The corresponding orbits look much like the orbits for $n=9$ in the left-hand panel of Fig. 5. However, their detailed shape as well as the "surfing mecha-

nism" described in Ref. [46] are contingent on the presence and shape of the atomic potential. In the present case, it is remarkable that the ninth harmonic still yields to the SPA and allows the identification of quantum orbits, even though its generation appears to be entirely in the quantum regime.

IV. THE UNIFORM APPROXIMATION

As we have shown, the SPA fails for harmonic orders near the cutoff when the two solutions of a given pair approach each other (see Fig. 1). After some critical point, which is very close to the cutoff energy, one of the solutions of this pair must be discarded because its contribution to the harmonic-emission rate starts to diverge. This solution is unphysical: a continuous deformation of the original real multidimensional $t, t_0, \mathbf{q}$ integration contour into complex space will never reach it. In our notation, the solutions $\alpha\beta m$ for which $\alpha=-\beta$ have to be dropped after the cutoff. The position n_c of the mentioned critical point can be defined in a mathematically more rigorous way by the condition for the so-called anti-Stokes transition [35]

$$\mathrm{Im}S_{n_c,1\beta m}=\mathrm{Im}S_{n_c,-1\beta m}, \tag{13}$$

where S_{ns} is given by Eq. (10) with $s\equiv\alpha\beta m$, $m=0,1,2,\ldots$ for $\beta=-1$, and $m=1,2,\ldots,$ for $\beta=1$. In the theory of asymptotic expansion of integrals [47,48], there is a method—the uniform approximation—that works in the case of coalescing saddle points. In our case of two coalescing points, this method leads to an expression that contains Airy functions. Not going into details, we here reproduce the final result obtained using this uniform approximation [35,47–49]

$$\begin{aligned} M_{n,\beta m} &= \sum_{\alpha=\pm 1} A_{n,\alpha\beta m}\exp(iS_{n,\alpha\beta m}) \\ &= (6\pi S_-)^{1/2}\exp(iS_+ + i\pi/4) \\ &\quad\times\left[\frac{A_-}{\sqrt{z}}\mathrm{Ai}(-z)+i\frac{A_+}{z}\mathrm{Ai}'(-z)\right], \end{aligned} \tag{14}$$

where $z=(3S_-/2)^{2/3}$, and the quantities

$$\begin{aligned} 2S_\pm &= S_{n,1\beta m}\pm S_{n,-1\beta m}, \\ 2A_\pm &= A_{n,1\beta m}\pm iA_{n,-1\beta m} \end{aligned} \tag{15}$$

are related to the actions (10) and the weights (9) of the saddle points. Equation (14) is valid for $n<n_c$. For $n>n_c$, the argument z must be replaced by $z\exp(i2\beta\pi/3)$. That way, the proper branch of the Airy functions is selected, which drops the unphysical saddle point. Also, for $n>n_c$, $M_{n,\beta m}$ should change its sign. With the help of the asymptotics of the Airy functions [50], it is possible to verify that $M_{n,\beta m}$ indeed reduces to the sum of the two saddle-point contributions for $n<n_c$, or to only one of them for $n>n_c$. Hence, the standard saddle-point representation (8) is retrieved when the saddle points are sufficiently well separated.

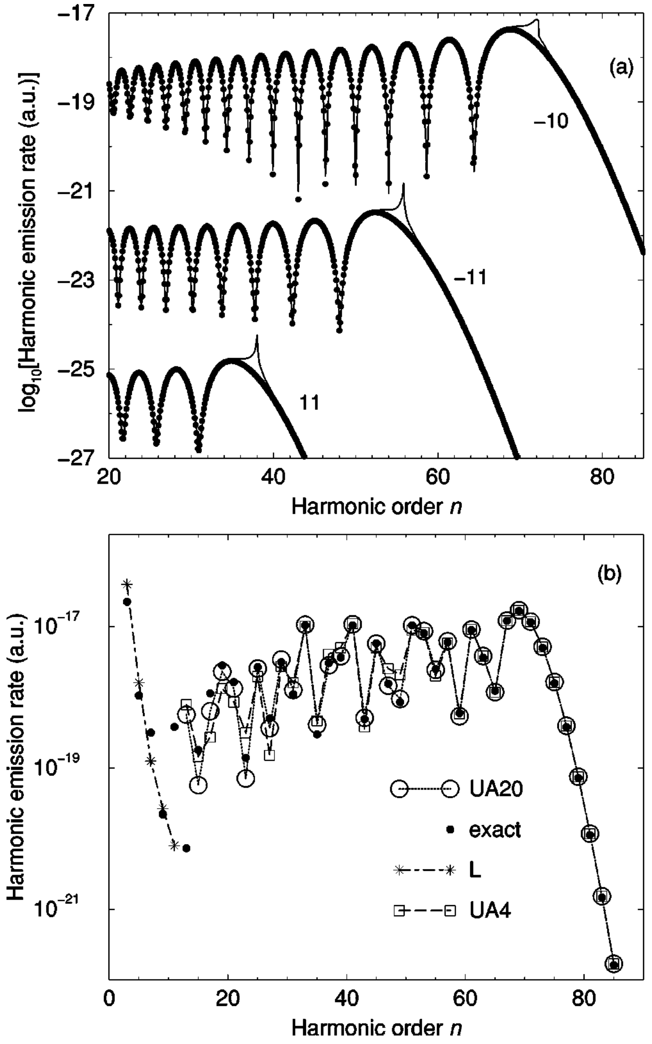

FIG. 6. (a) Comparison of the partial harmonic-emission rates obtained using the uniform approximation (filled circles), Eq. (14), with the saddle-point results summed over α, for three different values of the numbers βm, as indicated in the figure. The spectra with $m=1$ have been shifted down for better visibility. (b) Comparison of the harmonic spectrum obtained using numerical integration ("exact" results) with the spectrum obtained using the uniform approximation with 4 and 20 pairs of solutions taken into account, presented similarly as in Fig. 3. The atomic and laser parameters are the same as in Figs. 1–5.

Figure 6 demonstrates the quality of the uniform approximation. The artifacts of the saddle-point approximation around the cutoffs have been eliminated [Fig. 6(a)], and the uniform-approximation results are closer to the exact results [Fig. 6(b)]. In addition to the cutoff region, particular improvements are noticeable around $n=(I_\mathrm{P}+2U_\mathrm{P})/\omega\approx 47$ where, as we shall see below, the cutoffs for higher values of m accumulate, introducing significant error in the SPA results. For low harmonics, the uniform approximation does not give adequate results, due to the different nature of the critical point at $n\omega=I_\mathrm{P}$, where all partial contributions accumulate and tend to zero.

V. APPROXIMATE ANALYTICAL SOLUTIONS

An approximate solution of the system (7) can be obtained by supposing that the momentum $k=(\sin\varphi_0-\sin\varphi)/(\varphi-\varphi_0)$ is small. This is true for long travel times $\tau=\mathrm{Re}(\varphi-\varphi_0)/\omega$. We will consider the case $n\omega>I_{\mathrm{P}}$, for which Eq. (7b) reduces to $k+\cos\varphi=\pm\gamma_n$, $\gamma_n>0$. For the "$-$" sign and for $\varphi\in[0,2\pi]$, we have two solutions

$$\varphi=(1-\alpha)\pi+\alpha\arccos(-\gamma_n-k),\quad \alpha=\pm1, \tag{16}$$

where, for real k and $|k|<\gamma_n$, we have $\varphi_{\alpha=+1}\in(\pi/2,\pi]$ and $\varphi_{\alpha=-1}\in[\pi,3\pi/2)$.

If we shift these solutions by $\alpha\pi$, we have $\cos\varphi=-k(\varphi,\varphi_0)-\gamma_n\to\cos(\varphi+\alpha\pi)=-k(\varphi+\alpha\pi,\varphi_0+\alpha\pi)-\gamma_n$, which reduces exactly to the initial equation $k+\cos\varphi=\pm\gamma_n$, with the "$+$" sign. Therefore, the second set of the solutions is obtained by shifting the solution (16) by $\alpha\pi$, with a simultaneous shift of φ_0 by $\alpha\pi$. This is because the linearly polarized field (2) satisfies $A(t+T/2)=-A(t)$, which implies $d(t+T/2)=-d(t)$ for the dipole moment. Including these solutions in the calculation of the emission rates (8) yields a factor of $1-\exp(in\alpha\pi)$. It makes sure that no even harmonics are produced. Since, however, only odd-integer harmonics are physically relevant, we can just discard this second set of solutions and multiply the rate (8) by a factor of 4.

Equation (7c), after expansion in powers of k, reduces to $\cos(\mathrm{Re}\varphi_0)=-k/\sqrt{1+\gamma^2}$, $\mathrm{Im}\varphi_0=\mathrm{arcsinh}\gamma$. The general solution is $\mathrm{Re}\varphi_0=\pm\arccos(-k/\sqrt{1+\gamma^2})-2r\pi$, $r=0,\pm1,\pm2,\ldots$. The principal value of the arccos function in the expression for $\mathrm{Re}\varphi_0$ is between 0 and $\pi/2$ for $k\leqslant0$ and between $\pi/2$ and π for $k>0$. Expanding the arccos function in powers of k, we get the final result [for $\mathrm{Re}(\varphi-\varphi_0)>0$]

$$\varphi_0=\beta\left(\frac{\pi}{2}+\frac{k}{\sqrt{1+\gamma^2}}\right)-2m\pi+i\,\mathrm{arcsinh}\gamma,\quad \beta=\pm1, \tag{17}$$

where $m=1,2,\ldots$ for $\beta=+1$, and $m=0,1,2,\ldots$ for $\beta=-1$. Letting $k^{(0)}=0$ in Eqs. (16) and (17), we obtain the zeroth-order approximations $\varphi^{(0)}$ and $\varphi_0^{(0)}$. Introducing these solutions into the expression for k, we obtain the first-order approximation

$$k^{(1)}=\frac{\beta\sqrt{1+\gamma^2}-\alpha\sqrt{1-\gamma_n^2}}{2m\pi}, \tag{18}$$

which holds for $2m\pi\gg1$. Replacing k by $k^{(1)}$ in Eqs. (16) and (17) gives the required approximate analytical solution for φ and φ_0. In Eq. (18), the factor $\sqrt{1-\gamma_n^2}$ is real if $n\omega\leqslant I_{\mathrm{P}}+2U_{\mathrm{P}}$. Therefore, the above approximate result can be applied for $I_{\mathrm{P}}<n\omega\leqslant I_{\mathrm{P}}+2U_{\mathrm{P}}$, i.e., at the beginning and in the middle part of the HHG plateau. A better first-order approximation can be obtained by calculating $k^{(1)}$ from Eq. (7a) with $\varphi_0=\varphi_0^{(0)}$ and $\varphi=\varphi^{(0)}$, and substituting the $k^{(1)}$ so obtained into the relations $\varphi_0^{(1)}=\varphi_0^{(0)}+\beta k^{(1)}/\sqrt{1+\gamma^2}$ and $\varphi^{(1)}=\varphi^{(0)}+\alpha k^{(1)}/\sqrt{1-\gamma_n^2}$.

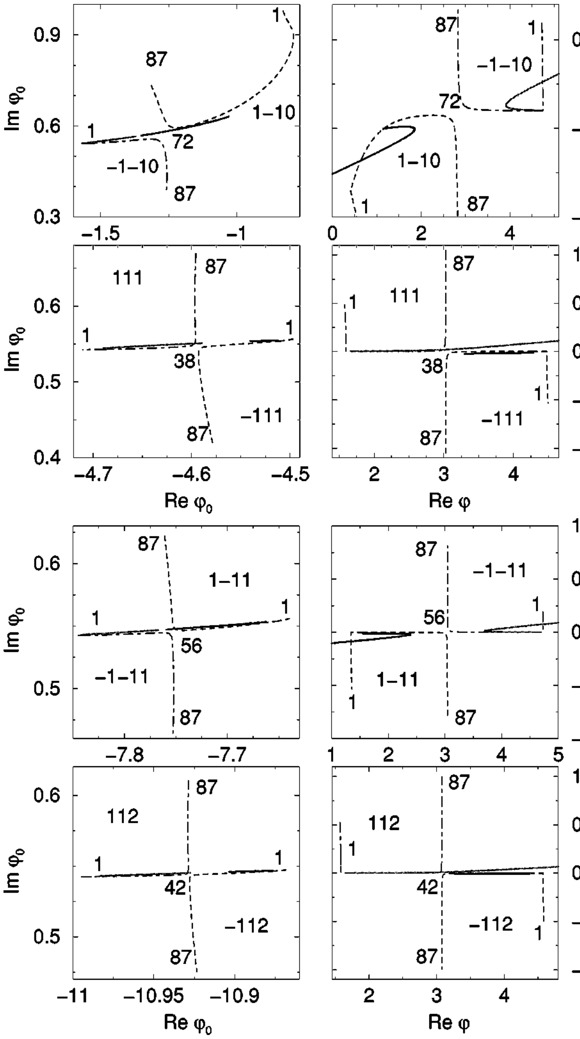

FIG. 7. Comparison of the approximate (solid lines) and the exact (dashed and dot-dashed lines) solutions of the saddle-point equations for the parameters of Fig. 1. The approximate solutions are presented with the harmonic order n as a continuous parameter in the interval $11.6=I_{\mathrm{P}}/\omega<n\leqslant(I_{\mathrm{P}}+2U_{\mathrm{P}})/\omega=47.4$. For the solutions $\alpha\beta m=-111$ and -112, the harmonic order is less than 38 and 42, respectively.

A comparison of these approximate solutions with those presented in Fig. 1 is shown in Fig. 7. One can see that, for increasing m, the analytical solutions become a good approximation, as expected. A comparison of the corresponding harmonic-emission rates with each other is shown in Fig. 8. Already for $m=2$, the harmonic-emission rates obtained from the approximate analytical solutions are a good approximation. For $m>2$, one can safely use this approximation. A characteristic feature of these approximate spectra is that the sharp peaks, where the SPA fails [35], are shifted to higher values of n (see the right-hand panels in Fig. 8). With the increase of m, this shift becomes smaller. The exact positions of these peaks can be calculated. In Refs. [42,44] it was found that, for our present parameters $\beta m=-10$, 11, -11 one has, respectively, $n_c\omega=3.173U_{\mathrm{P}}+1.325I_{\mathrm{P}}$, $1.542U_{\mathrm{P}}+0.884I_{\mathrm{P}}$, $2.404U_{\mathrm{P}}+1.102I_{\mathrm{P}}$, which for the parameters of Figs. 1–8 corresponds to $n_c=72.28$, 37.91,

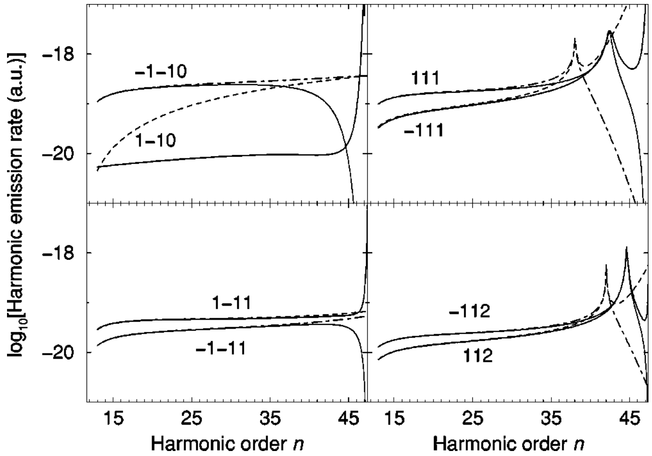

FIG. 8. Comparison of the partial harmonic-emission rates obtained using the approximate analytical solutions of the saddle-point equations (solid lines) with those presented in Fig. 4(a) that are obtained using the exact solutions (dashed and dot-dashed lines). The numbers $\alpha\beta m$ are indicated next to the corresponding curves.

55.90. For higher values of m, the position of the peaks is lower (higher) for $\beta=+1$ (-1). The values of $n_c(\beta,m)$ are arranged according to $n_c(-1,m)>n_c(-1,m+1)$, $n_c(1,m)<n_c(1,m+1)$, $m=0,1,2,\ldots$. Therefore, we expect that for $I_{\mathrm{P}}/\omega<n<n_c(1,1)$, i.e., $13\leqslant n\leqslant 37$ in our present case, we can safely use the SPA. For $m\geqslant 2$, the analytical solutions presented in this section can be used. If we calculate the harmonic-emission rates using the uniform approximation [35] for, say, $m\leqslant 4$, and the approximate analytical solutions for $m>4$, then we can obtain a harmonic spectrum up to $n=45$ that should be in excellent agreement with the "exact" results. This method will be used in the following sections to consider the enhancement of HHG at channel closings, for which the contribution of high values of m has to be taken into account.

VI. ENHANCEMENT OF HIGH-ORDER HARMONIC GENERATION AT CHANNEL CLOSINGS

In the Introduction, we mentioned that the resonancelike enhancement of HHG is observed at intensities that satisfy the resonance condition

$$R=\frac{I_{\mathrm{P}}+U_{\mathrm{P}}}{\omega}=l, \tag{19}$$

with l integer. Using our analytical solution, we can explain this resonance condition and, furthermore, we can predict for which laser and atomic parameters this enhancement is more significant. In order to do this, we calculate analytically the real part of the action (10). The procedure is very similar to the corresponding analysis for ATI [24]. The phase of each term $A_n\exp(iS_n)$ in the sum in Eq. (8), up to a constant, is given by

$$\mathrm{Re}S_n+\Phi_{A_n}=-2mR\pi+\beta R\frac{\pi}{2}+\frac{U_{\mathrm{P}}}{\omega}\alpha\gamma_n\sqrt{1-\gamma_n^2}+(n-R)[(1-\alpha)\pi+\alpha\arccos(-\gamma_n)]+\alpha\frac{\pi}{4}. \tag{20}$$

We have neglected contributions of the order $(2m\pi)^{-1}$. The term $\alpha\pi/4$ comes from the phase of $F_s^{-1/2}$ in Eq. (8) because the dominant term in F is

$$F\propto(k+\cos\varphi)(k+\cos\varphi_0)\sin\varphi\sin\varphi_0(\varphi-\varphi_0)$$
$$\propto(-\gamma_n)(-i\beta\gamma)\alpha\sqrt{1-\gamma_n^2}\beta\sqrt{1+\gamma^2}2m\pi,$$

which is proportional to α. We can now investigate, under which conditions the contributions of different quantum orbits $\alpha\beta m$ add constructively, generating the enhancement.

Two orbits $\alpha\beta m$ and $\alpha'\beta'm'$ interfere constructively when $\Delta_n(\alpha\beta m|\alpha'\beta'm')\equiv\mathrm{Re}S_{n,\alpha\beta m}-\mathrm{Re}S_{n,\alpha'\beta'm'}+(\alpha-\alpha')\pi/4=2r\pi$, with r integer. From Eq. (20), it is clear that $\Delta_n(\alpha\beta m+1|\alpha\beta m)=2R\pi$ so that orbits with the same α and β and different m add constructively if the resonance condition (19) is satisfied. Suppose now that $R=l$. Then, from Eq. (20), we have $\Delta_n(\alpha 1m|\alpha-1m)=l\pi$, so that, for fixed α and with $R=l$, the contributions of different β (that is, the two pairs of orbits with start times within the same cycle of the field) add constructively for l even and destructively for l odd. The situation is more complicated for orbits with opposite α. Suppose again that the resonance condition (19) is fulfilled. In this case, we have $\Delta_n(1\beta m|-1\beta m)=2(n-l)[\arccos(-\gamma_n)-\pi]+2U_{\mathrm{P}}\gamma_n\sqrt{1-\gamma_n^2}/\omega+\pi/2$. Therefore, for fixed β and for $R=l$, the contributions of opposite α (that is, the long and the short orbits of a given pair) add constructively only for those particular harmonics n that render the quantity

$$C_n=\frac{n-l}{\pi}\arccos(-\gamma_n)+\frac{U_{\mathrm{P}}}{\omega}\frac{\gamma_n}{\pi}\sqrt{1-\gamma_n^2}+\frac{1}{4} \tag{21}$$

integer. The quantity γ_n is defined below Eqs. (7). This condition is very similar to the corresponding condition for the enhancements of high-order ATI [24] that predicts enhancements of groups of ATI peaks [13–15].

Next, using some examples, we will investigate the magnitude of the enhancement and for which harmonics it appears. In Fig. 9, we show harmonic spectra obtained using numerical integration ("exact" results) for two laser intensities that differ by only about 1%. The lower intensity I_R corresponds to the resonance condition (19) with $R=l=22$. The corresponding emission rates of the harmonics between $n=11$ and $n=31$ exceed by almost one order of magnitude those harmonics which are generated by the slightly higher intensity I. The energies of the enhanced harmonics lie in the interval

$$I_{\mathrm{P}}<n\omega<I_{\mathrm{P}}+2U_{\mathrm{P}} \tag{22}$$

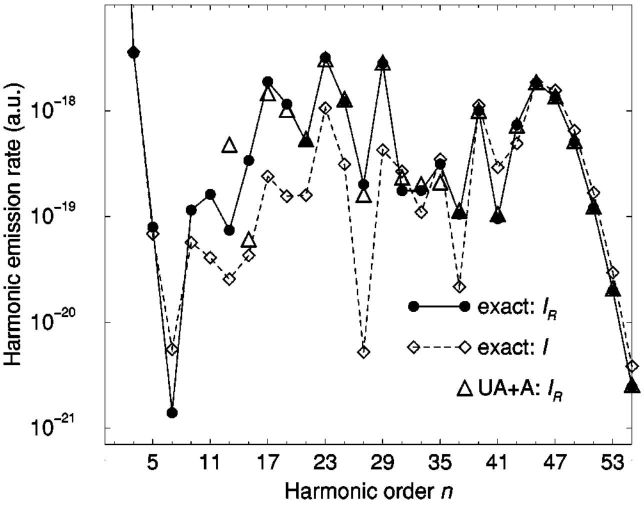

FIG. 9. Harmonic-emission rates in dependence on the harmonic order for two closely adjacent intensities: $I=1.17\times 10^{14}$ W/cm^2 and $I_R=1.158\times 10^{14}$ W/cm^2. The results are obtained by numerical integration ("exact"). The lower intensity I_R corresponds to the resonance condition (19) with $R=l=22$. For comparison, results for I_R, obtained using the uniform approximation combined with the analytical solutions ("UA+A"), are also presented. The photon and the atomic ionization energy are $\omega=1.17$ eV and $I_{\rm P}=13.6$ eV, respectively.

as expected from the analytical theory presented in the preceding section.

It is interesting to observe that in the integral (6), the numerical integration over τ for the case of the resonant intensity had to be extended to very large values in order to obtain good convergence. Namely, for the nonresonant case of the intensity I, it is usually sufficient to terminate the integration over τ at $5T$, while for the resonant case, one has to go at least one order of magnitude higher (for the calculation presented, the upper limit of this integration was $80T$). The reason is, of course, related to the significance of the orbits with long travel times at channel closings. In the integral (6), this enters through the absence at channel closings of oscillating factors that otherwise allow one to terminate the integration at comparatively short times τ [28]. At channel closings, it is only the factor of $\tau^{-3/2}$ in the integrand that brings about convergence. This peculiarity makes the "exact" calculations much more time consuming and, therefore, inconvenient for practical applications. Fortunately, the methods developed in this paper allow us to calculate the harmonic-emission rates within a few seconds even for the resonant intensities. In Fig. 9, such results for the resonant intensity I_R, obtained using the uniform approximation combined with the analytical solutions (denoted by "UA+A" and identified by the open triangles) agree very well with the "exact" results.

The methods developed so far allow us to analyze the resonance enhancement or the channel-closing effect in more detail. In Fig. 10, we present the dependence of harmonic-emission rates on the parameter $R=(I_{\rm P}+U_{\rm P})/\omega$ for the harmonic orders $n=17$, 23, 29, and 35. For the top panel ($n=35$), the results obtained using the uniform approximation with $m=2$ (dot-dashed line) are approximately equal to the more precise results obtained using the uniform approximation with $m=5$ combined with the analytical results including orbits up to $m=40$ (solid line). No channel-closing-related effects are visible, in agreement with the fact that the 35th harmonic lies outside the interval (22). Maxima do appear slightly below $R=22$ and $R=23$. They are generated by shorter quantum orbits and will be discussed below. In the other panels of Fig. 10, the characteristic resonant maxima are clearly visible. As expected, they are particularly sharply defined for even values of R, broader for odd values. The dot-dashed curves, which correspond to the contributions of low m, deviate from the exact results particularly at the channel closings.

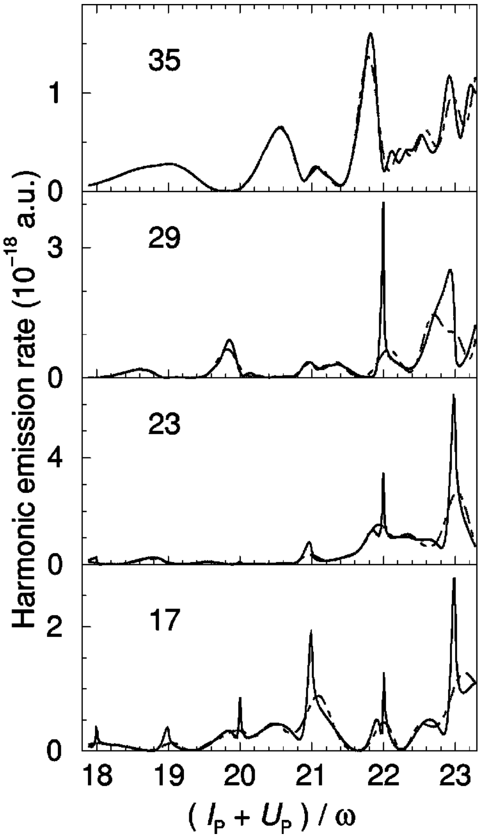

FIG. 10. Harmonic-emission rates as functions of the laser-field intensity, expressed by the parameter $R=(I_{\rm P}+U_{\rm P})/\omega$, for the harmonic orders $n=17$, 23, 29, and 35, from bottom to top, respectively. The dot-dashed lines specify the results obtained using the uniform approximation with $m\leqslant 2$, while the solid lines correspond to the results of the uniform approximation with $m\leqslant 5$ combined with the analytical results with m up to 40. The laser frequency is $\omega=1.17$ eV, and the ionization energy is $I_{\rm P}=13.6$ eV.

In Figs. 11 and 12, we show illustrations of the channel-closing effect for higher laser intensities. One can see that, for $R=30$ (the curve with filled circles in Fig. 11), the enhancement in the region given by Eq. (22), which, for the present case, corresponds to $11<n<49$, is more than one order of magnitude. In Fig. 12, we present data similar to those of Fig. 10, but for higher laser-field intensities. For $R=28$, the 25th harmonic exhibits a sharp spike, while for the

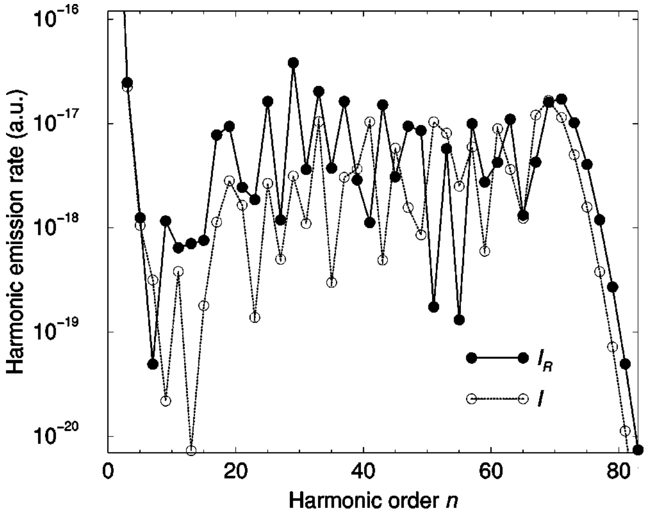

FIG. 11. Harmonic-emission rates as functions of the harmonic order for two closely adjacent intensities, $I=2\times10^{14}$ W/cm^2 and $I_R=2.05\times10^{14}$ W/cm^2, where the second intensity corresponds to $R=l=30$. The other parameters are as in Fig. 9.

33rd harmonic this is smaller, and for $n=43$, it is completely absent. For the odd-channel closing $R=29$, the 25th harmonic exhibits a peak, the harmonics $n=33$, a pronounced maximum just below $R=29$, and the harmonic 43, a small peak as well as a broad maximum at somewhat lower intensity. Finally, for $R=30$, all three harmonics exhibit sharp peaks. For $n=33$, one again observes a well developed maximum just below the channel closing. The comparatively broad maxima just below channel closings will be more closely considered in the following section.

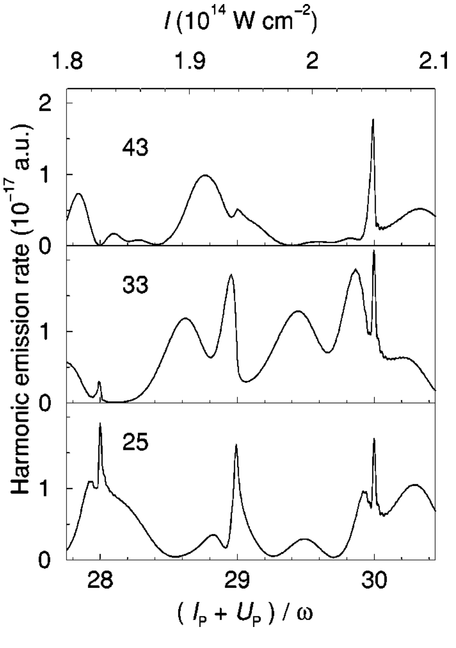

FIG. 12. Harmonic-emission rates as functions of the parameter $R=(I_P+U_P)/\omega$, for the harmonic orders $n=25$, 33, and 43, from bottom to top, respectively. The corresponding laser-field intensity is given at the top of the figure. The other parameters are as in Fig. 10.

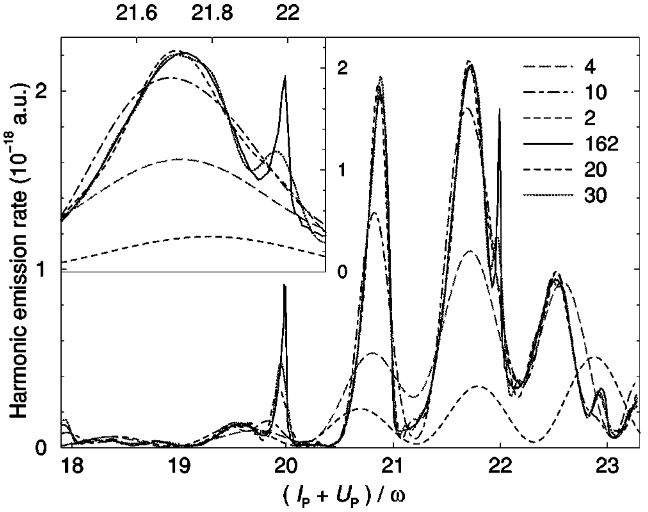

FIG. 13. Harmonic-emission rate as a function of $R=(I_P+U_P)/\omega$, for the harmonic order $n=25$. The data presented are for different values of the numbers m_1 and m_2 in Eq. (23): $m_1=5$, $m_2=40$ (solid curve, 162 orbits), $m_1=2$, $m_2=0$ (dot-dashed curve, ten orbits), and $m_1=m_2=0$ (dashed curve, two orbits). The data for 4, 20, and 30 orbits are also presented as denoted in the legend. The other parameters are as in Fig. 10. The inset displays an enlargement of the features at and below the channel closing at $R=22$, with the scales at the right and upper margin.

VII. ANALYSIS OF HHG IN TERMS OF LONG QUANTUM ORBITS: AN EXAMPLE

The formalism described in the preceding sections enables us to analyze HHG in terms of the contributions of particular quantum orbits denoted by the numbers $\alpha\beta m$. This can be done in many different ways. In this section, we will present an example of this analysis. Figure 13 shows the 25th-harmonic-emission rate as a function of the laser intensity, expressed through the parameter $R=(I_P+U_P)/\omega$. The results presented are obtained using the expression (8) for the harmonic-emission rate with

$$\sum_s A_{ns}\exp(iS_{ns}) = \sum_{m=0}^{m_1}\sum_{\beta=\pm1} M_{n,\beta m} + \sum_{m=m_1+1}^{m_2}\sum_{\alpha,\beta=\pm1} A^{(1)}_{n\alpha\beta m}\exp(iS^{(1)}_{n\alpha\beta m}). \tag{23}$$

In the first sum, the matrix element $M_{n,\beta m}$ is calculated by the uniform approximation, Eq. (14). The second sum contains the contributions of the orbits with higher m, obtained by using the analytical results in the first-order approximation, as explained below Eq. (18). The solid line in Fig. 13 corresponds to $m_1=5$ and $m_2=40$, which encompasses 162 orbits. The dot-dashed and the dashed line has been calculated for $m_1=2$ (ten orbits) and $m_1=0$ (two orbits), respectively, and the second sum was disregarded in either case. The case $m_1=0$ comprises only the two shortest orbits $\alpha\beta m=1-10$, from $-1-10$, which are often, in the literature, referred to as *the short orbit* and *the long orbit*. It is

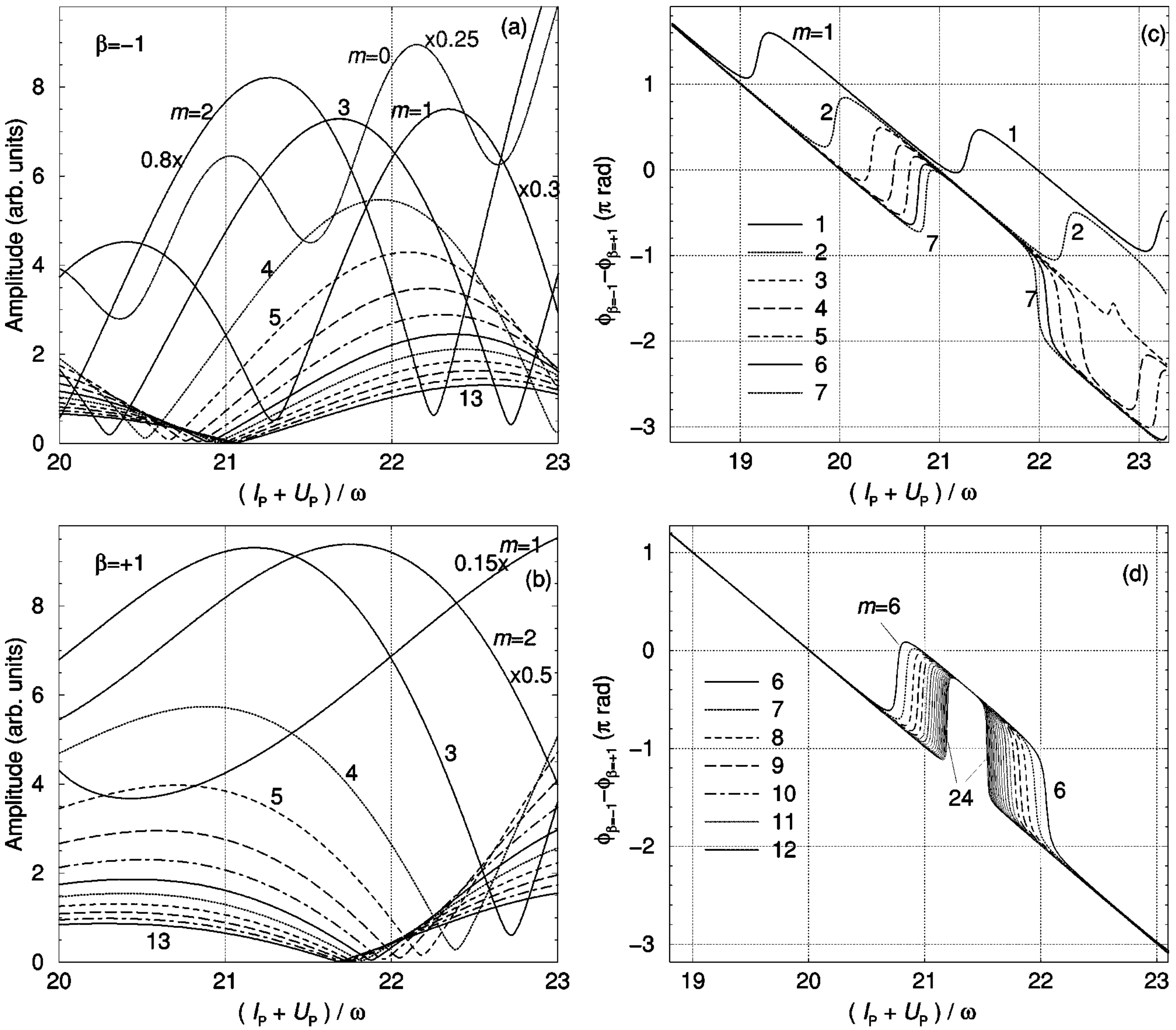

FIG. 14. Partial amplitudes [(a) and (b)] and relative phases [(c) and (d)] of the quantum-orbit contributions to the harmonic-emission rate for the 25th harmonic (see the text for the precise definition) for various values of m, as indicated in the panels, as functions of the parameter $R=(I_P+U_P)/\omega$. The parameters are as in Fig. 10. (a) Partial amplitudes for $\beta=-1$; (b) partial amplitudes for $\beta=+1$; (c) relative phases for $1\leqslant m\leqslant 7$; (d) relative phases for $6\leqslant m\leqslant 24$. The partial amplitudes for $m=0,1$ and 2 in (a) and (b) have been multiplied with a constant factor as specified.

obvious that these two cannot reproduce the exact result, which is practically very well approximated by the solid line. Better approximations are obtained if more orbits are included (for example, $m_1=2$ implies $\beta m=-10,11,-11,12,-12$ and $\alpha=\pm 1$, which gives ten orbits).

Two features of Fig. 13 are very conspicuous: the sharp spikes at the even channel closings $R=20$ and $R=22$, and the strong maxima slightly below $R=21$ and $R=22$. These maxima are much broader than the spikes, and as we can see for $R=22$, they are clearly distinguished from the former. They are of the same type as those that we observed already in Figs. 10 and 12. Figure 13 shows that these peaks cannot be explained in terms of just two orbits (dashed curve) but can be qualitatively understood in terms of ten orbits (dot-dashed curve). We conclude that the main contribution to these peaks comes from relatively low values of m. In contrast, the even-channel-closing spikes require at least 30 orbits to become just only noticeable and many more to produce the sharp spike (cf. the inset of Fig. 13). On the other hand, the features of the harmonics in the upper end of the plateau and in the cutoff region (see, e.g., Fig. 10 for $n=35$) require for a qualitative understanding just the two shortest orbits.

In order to gain further insight into these results, we present in Figs. 14(a) and 14(b) partial amplitudes $|\Sigma_{\alpha=\pm 1}A_{n\alpha\beta m}\exp(iS_{n\alpha\beta m})|$ from the quantum-orbit decomposition (23) for various values of m and (a) $\beta=-1$, and (b) $\beta=+1$, and in Figs. 14(c) and 14(d), the relative phase $\phi_{\beta=-1}-\phi_{\beta=+1}$, where ϕ_β is the phase of $\Sigma_{\alpha=\pm 1}A_{n\alpha\beta m}\exp(iS_{n\alpha\beta m})$. From Figs. 14(a) and 14(b), we see that the amplitudes for $m=2$ for $\beta=+1$ and $m=3$ for $\beta=-1$ have maxima slightly below $R=22$. Apparently, the superposition of these amplitudes with those from $m=0$ and $m=1$ generates the above-mentioned pronounced maxima below $R=21$ and $R=22$. Other features of Figs. 14(a) and 14(b) that ought to be mentioned include: (i) For increasing m, the partial amplitudes decrease very slowly. This decrease is largely due to wave-function spreading, as expressed in the $\tau^{-3/2}$ decrease of the integrand of the integral (6). If all of these amplitudes interfere constructively, a very strong and sharp enhancement results. This is what happens at the spikes to be discussed below. (ii) The rather sudden dips of the partial amplitudes [e.g., those below $R=21$ in Fig. 14(a) as well as at $R=22.7$ for $m=3$] are due to destructive interference of the long and the short orbits ($\alpha=\pm 1$) for fixed β and m. This is the same mechanism that generates the interference dips in Fig. 6. (iii) Comparison of Figs. 14(a) and (b) with (c) and 14(d) shows that for those values of R, where the partial amplitudes for either $\beta=1$ or $\beta=-1$ assumes an interference dip, their relative phase jumps by $\pm\pi$. This generates the patterns that dominate Figs. 14(c) and 14(d), with interesting consequences for the channel-closing spikes, to be discussed next.

The overall linear slope $-\pi$ of the relative phases plotted in Figs. 14(c) and 14(d) is the consequence of the term $\beta R\pi/2$ on the right-hand side of the phase (20). Let us consider the channel closings $R=20$, 21, and 22, separately. According to Fig. 13, at $R=20$, the 25th harmonic displays a moderately sharp spike on little background. Indeed, Figs. 14(c) and 14(d) show that at $R=20$, the contributions of $m=1$ and $m=2$ are each approximately out of phase, while all contributions with higher m are pairwise exactly in phase. Next, exactly at the odd-channel closing $R=21$, the harmonic amplitude of Fig. 13 does not exhibit any noticeable spike. Consulting Figs. 14(c) and 14(d), we observe that the contributions with $m\leqslant 7$ are approximately in phase, for $7<m\lesssim 13$ there are various phases, while for $m\gtrsim 14$ the contributions are pairwise exactly out of phase. Consequently, no channel-closing spike develops as expected for an odd-channel closing. Finally, for $R=22$, the situation is opposite: the contributions with low m (except $m=1$) are pairwise more or less out of phase, while those with high m, starting with $m\approx 7$, are precisely in phase. This generates the very sharp spike that is visible in Fig. 13.

VIII. DISCUSSION AND CONCLUSIONS

Many features of the Lewenstein model of high-order harmonic generation can be understood in terms of the properties and the interplay of just two quantum orbits, those two that have the shortest travel time. These features include, on the single-atom level, the existence and value of the cutoff as well as the smooth behavior of the spectrum above this cutoff and its ragged structure below. In the collective response, depending on the focal conditions, these two orbits can be and are separated, which produces a multitude of effects [1,10]. In this paper, we have employed various approximations, notably the uniform approximation and an analytic approximation applicable for the orbits with very long travel times, in order to investigate in detail, on the single-atom level, the properties of the long orbits and their significance for the spectrum.

The classical cutoffs of the long orbits converge in the limit of long travel times towards I_P+2U_P. Well above this energy, the harmonic spectrum can be adequately described by the two shortest orbits, with their cutoff—the highest of all orbits—at the energy $I_P+3.17U_P$. Since orbits make their strongest contribution right before their classical cutoffs, we expect and we do find the most pronounced long-orbit effects in the region around I_P+2U_P. It is here, where the extremely sharp spikes at intensities that correspond to even-channel closings are best developed. We found that an extremely large number of orbits (about 100, corresponding to travel times up to 25 cycles) is required to generate these sharp spikes. This would seem to put the experimental relevance of the channel-closing spikes into question, in addition to the unanswered question of whether these spikes are still observable after propagation.

We identified another manifestation of medium-long orbits (about the ten shortest orbits, traveling approximately up to three cycles) in the harmonic-energy region around I_P+2U_P: well developed enhancements at intensities just below the channel closings. These are quite pronounced, but much less sharply defined than the actual channel-closing spikes. In a calculation with a not too dense intensity mesh, they might easily be mistaken for the former. For their existence, it does not matter whether the associated channel closing is even or odd. Whether or not these enhancements have practical relevance, depends on their phase-matching behavior, which has not yet been investigated.

In comparison with the analogous channel-closing enhancements in high-order ATI, the enhancements in HHG are much sharper. This can be traced to the quantity C_n [Eq. (21); this is the α-dependent part of the real part (20) of the action], which varies more rapidly as a function of the harmonic order n and the laser intensity than the corresponding term in the action for high-order ATI as a function of the electron energy [24].

The idea that orbits with travel times between ionization and recombination of many cycles of the driving laser field make, under appropriate circumstances, significant contributions to the observed harmonic-generation spectrum is very intriguing. The question is near at hand whether this might be an artifact of the strong-field approximation, which neglects the Coulomb potential of the ion while the electron is traveling. While a precise answer to this question is not known, it is interesting to refer to Muller's purely numerical simulations of high-order ATI on the basis of the three-dimensional time-dependent Schrödinger equation [18,19]. These, of course, take into account a realistic binding potential. ATI spectra that come out of these calculations look much like spectra computed in the context of quantum orbits and the strong-field approximation and display virtually the same intensity-dependent enhancements [16,20,24]. In particular, inspection of the time evolution of Muller's simulations has established the connection between long electron orbits extending over many cycles of the laser field and the intensity-dependent enhancements of groups of ATI peaks [18,19]. In the exact numerical simulations, the enhancements are not related to the channel closings, but rather to multiphoton resonances with ponderomotively upshifted Rydberg states. This has, however, little effect on the shape of the enhancement.

Recently, the harmonic spectrum generated by a laser-irradiated atom modeled by a zero-range potential has been calculated exactly on the basis of an intricate exact analytic solution [23]. The results agree qualitatively and, in so far as this has been tested, quantitatively with our present and with earlier results [28,30]. This is fortunate because it removes any doubts that may have remained, questioning the legitimacy of the strong-field approximation in the Lewenstein model and other less severe approximations made in the zero-range potential model [28,30]. The analytic solution of Ref. [23] is set in the context of the quasienergy formalism and does not yield immediate insight into the temporal evolution of harmonic emission. It interprets the intensity-dependent spikes in intense-laser-atom processes as a special manifestation of the general phenomenon of threshold anomalies that were discovered in time-independent scattering theory [25,26]. The intensity-dependent enhancements of ATI have been analyzed in this context, too [22,27].

Finally, we should like to reemphasize the peculiar mechanism by which channel closings, which are genuine quantum features, materialize in a semiclassical approximation scheme: no particular quantum orbit will show any evidence of a channel closing. It is only their coherent superposition that does, owing to their intensity-dependent relative phases.

ACKNOWLEDGMENTS

We are indebted to C. Figueira de Morisson Faria for discussions. D.B.M. gratefully acknowledges support by the VolkswagenStiftung.

---

[1] P. Salières, A. L'Huillier, Ph. Antoine, and M. Lewenstein, Adv. At., Mol., Opt. Phys. **41**, 83 (1999).

[2] C.J. Joachain, M. Dörr, and N. Kylstra, Adv. At., Mol., Opt. Phys. **42**, 225 (2000).

[3] T. Brabec and F. Krausz, Rev. Mod. Phys. **72**, 545 (2000).

[4] W. Becker, F. Grasbon, R. Kopold, D.B. Milošević, G.G. Paulus, and H. Walther, Adv. At., Mol., Opt. Phys. **48**, 35 (2002).

[5] M. Lewenstein, Ph. Balcou, M.Yu. Ivanov, A. L'Huillier, and P.B. Corkum, Phys. Rev. A **49**, 2117 (1994); A. L'Huillier, M. Lewenstein, P. Salières, Ph. Balcou, M.Yu. Ivanov, J. Larsson, and C.G. Wahlstrom, *ibid.* **48**, R3433 (1993).

[6] M. Lewenstein, K.C. Kulander, K.J. Schafer, and P.H. Bucksbaum, Phys. Rev. A **51**, 1495 (1995).

[7] R. Kopold, D.B. Milošević, and W. Becker, Phys. Rev. Lett. **84**, 3831 (2000).

[8] P. Salières, B. Carré, L. Le Déroff, F. Grasbon, G.G. Paulus, H. Walther, R. Kopold, W. Becker, D.B. Milošević, A. Sanpera, and M. Lewenstein, Science **292**, 902 (2001).

[9] The term "quantum paths," as opposed to "quantum orbits," has often been used in the context of an approximation to the action of the quantum orbits, which underlies the analysis of Refs. [10,11].

[10] M. Bellini, C. Lyngå, A. Tozzi, M.B. Gaarde, T.W. Hänsch, A. L'Huillier, and C.-G. Wahlström, Phys. Rev. Lett. **81**, 297 (1998).

[11] M.B. Gaarde, F. Salin, E. Constant, Ph. Balcou, K.J. Schafer, K.C. Kulander, and A. L'Huillier, Phys. Rev. A **59**, 1367 (1999); Ph. Balcou, A.S. Dederichs, M.B. Gaarde, and A. L'Huillier, J. Phys. B **32**, 2973 (1999); D.G. Lee, H.J. Shin, Y.H. Cha, K.H. Hong, J.-H. Kim, and C.H. Nam, Phys. Rev. A **63**, 021801(R) (2001); J.-H. Kim, D.G. Lee, H.J. Shin, and C.H. Nam, *ibid.* **63**, 063403 (2001); M.B. Gaarde and K.J. Schafer, *ibid.* **65**, 031406(R) (2002).

[12] R. Bartels, S. Backus, E. Zeek, L. Misoguti, G. Vdovin, I.P. Christov, M.M. Murnane, and H.C. Kapteyn, Nature (London) **406**, 164 (2000); I.P. Christov, R. Bartels, H.C. Kapteyn, and M.M. Murnane, Phys. Rev. Lett. **86**, 5458 (2001).

[13] P. Hansch, M.A. Walker, and L.D. Van Woerkom, Phys. Rev. A **55**, R2535 (1997).

[14] M.P. Hertlein, P.H. Bucksbaum, and H.G. Muller, J. Phys. B **30**, L197 (1997).

[15] M.J. Nandor, M.A. Walker, L.D. Van Woerkom, and H.G. Muller, Phys. Rev. A **60**, R1771 (1999).

[16] G.G. Paulus, F. Grasbon, H. Walther, R. Kopold, and W. Becker, Phys. Rev. A **64**, 021401(R) (2001).

[17] E.S. Toma, Ph. Antoine, A. de Bohan, and H.G. Muller, J. Phys. B **32**, 5843 (1999).

[18] H.G. Muller and F.C. Kooiman, Phys. Rev. Lett. **81**, 1207 (1998).

[19] H.G. Muller, Phys. Rev. A **60**, 1341 (1999); Opt. Express **8**, 44 (2001).

[20] R. Kopold, W. Becker, M. Kleber, and G.G. Paulus, J. Phys. B **35**, 217 (2002).

[21] C. Figueira de Morisson Faria, R. Kopold, W. Becker, and J.M. Rost, Phys. Rev. A **65**, 023404 (2002).

[22] B. Borca, M.V. Frolov, N.L. Manakov, and A.F. Starace, Phys. Rev. Lett. **88**, 193001 (2002).

[23] B. Borca, A.F. Starace, A.V. Flegel, M.V. Frolov, and N.L. Manakov, Phys. Rev. A **65**, 051402(R) (2002).

[24] S.V. Popruzhenko, Ph.A. Korneev, S.P. Goreslavski, and W. Becker, Phys. Rev. Lett. **89**, 023001 (2002).

[25] E.P. Wigner, Phys. Rev. **73**, 1002 (1948).

[26] A.I. Baz', Zh. Éksp. Teor. Fiz. **33**, 923 (1957) [Sov. Phys. JETP **6**, 709 (1958)].

[27] F.H.M. Faisal and P. Scanzano, Phys. Rev. Lett. **68**, 2909 (1992).

[28] W. Becker, S. Long, and J.K. McIver, Phys. Rev. A **46**, R5334 (1992).

[29] W. Becker, S. Long, and J.K. McIver, Phys. Rev. A **50**, 1540 (1994).

[30] W. Becker, A. Lohr, S. Long, J.K. McIver, B.N. Chichkov, and B. Wellegehausen, Laser Phys. **7**, 88 (1997).

[31] M.Yu. Kuchiev and V.N. Ostrovsky, Phys. Rev. A **60**, 3111 (1999); J. Phys. B **32**, L189 (1999); **34**, 405 (2001).

[32] M.B. Gaarde and K.J. Schafer, Phys. Rev. A **64**, 013820 (2001).

[33] X. Chu, S.I. Chu, and C. Laughlin, Phys. Rev. A **64**, 013406 (2001).

[34] M. Plummer and C.J. Noble, J. Phys. B **35**, L51 (2002).

[35] C. Figueira de Morisson Faria, H. Schomerus, and W. Becker, Phys. Rev. A **66**, 043413 (2002).

[36] D.B. Milošević, in *Super-Intense Laser-Atom Physics*, edited by B. Piraux and K. Rzążewski (Kluwer Academic Publishers, The Netherlands, 2001) p. 229.

[37] L.V. Keldysh, Zh. Éksp. Teor. Fiz. **47**, 1945 (1964) [Sov. Phys. JETP **20**, 1307 (1965)]; F.H.M. Faisal, J. Phys. B **6**, L89 (1973); H.R. Reiss, Phys. Rev. A **22**, 1786 (1980); **42**, 1476 (1990).

[38] W. Becker, A. Lohr, M. Kleber, and M. Lewenstein, Phys. Rev. A **56**, 645 (1997).

[39] W. Becker, S. Long, and J.K. McIver, Phys. Rev. A **41**, 4112 (1990).

[40] R. Kopold, W. Becker, and D.B. Milošević, J. Mod. Opt. **49**, 1987 (2002). In Refs. [36,5] the time-dependent dipole has the form $\int dt_0 \langle \psi_0(t)|x G_L(t,t_0) x E(t_0)|\psi_0(t_0)\rangle$, where $E(t_0)\hat{\mathbf{e}}_x$ is the electric field vector. Using integration by parts, one can prove the equivalence of this form and the form (3). The equivalence has been confirmed by numerical evaluation.

[41] D.B. Milošević and B. Piraux, Phys. Rev. A **54**, 1522 (1996).

[42] D.B. Milošević, J. Phys. B **33**, 2479 (2000).

[43] For a laser field with pronounced elliptical polarization [7,42] or for an ultrastrong laser field [44] this is different: each region of the spectrum can be attributed to one particular pair of orbits. Since the strengths of the respective pairs are quite different, a multiplateau structure results. For above-threshold ionization, this has been observed in a recent experiment [8].

[44] D.B. Milošević, S. Hu, and W. Becker, Phys. Rev. A **63**, 011403(R) (2001); D.B. Milošević, S.X. Hu, and W. Becker, Laser Phys. **12**, 389 (2002).

[45] R. Kopold, W. Becker, and M. Kleber, Opt. Commun. **179**, 39 (2000).

[46] S.X. Hu, D.B. Milošević, W. Becker, and W. Sandner, Phys. Rev. A **64**, 013410 (2001); S.X. Hu, A.F. Starace, W. Becker, W. Sandner, and D.B. Milošević, J. Phys. B **35**, 627 (2002).

[47] N. Bleistein and R.A. Handelsman, *Asymptotic Expansions of Integrals* (Dover, New York, 1986).

[48] R. Wong, *Asymptotic Approximations of Integrals* (Academic Press, Boston, 1989).

[49] H. Schomerus and M. Sieber, J. Phys. A **30**, 4537 (1997).

[50] M. Abramovitz and I.A. Stegun, *Handbook of Mathematical Functions* (Dover, New York, 1965).